THE 3D DYNAMICS OF THE COSSERAT ROD AS APPLIED TO CONTINUUM ROBOTICS

By

Charles Rees Jones

A Dissertation
Submitted to the Faculty of
Mississippi State University
in Partial Fulfillment of the Requirements
for the Degree of Doctor of Philosophy
in Electrical Engineering
in the Department of Computer and Electrical Engineering

Mississippi State, Mississippi

August 6 2011

ProQuest LLC.
789 East Eisenhower Parkway
P.O. Box 1346
Ann Arbor, MI 48106 - 1346

THE 3D DYNAMICS OF THE COSSERAT ROD AS APPLIED TO CONTINUUM ROBOTICS

By

Charles Rees Jones

Approved:

Nicolas H. Younan Professor of Electrical and Computer Engineering, and Department Head (Major Professor)	Bryan A. Jones Associate Professor of Electrical and Computer Engineering (CoMajor Professor)
Ratnasingham Shivaji Professor of Mathematics (Committee Member)	Douglas Bammann Professor of Mechanical Engineering (Committee Member)
James E. Fowler Professor of Electrical and Computer Engineering, and Graduate Coordinator	Sarah A. Rajala Dean of the James Worth Bagley College of Engineering

Name: Charles Rees Jones

Date of Degree: August 6 , 2011

Institution: Mississippi State University

Major Field: Electrical Engineering

Major Professor: Dr. Nicolas H. Younan

Title of Study: THE 3D DYNAMICS OF THE COSSERAT ROD AS APPLIED TO CONTINUUM ROBOTICS

Pages in Study: 42

Candidate for Degree of Doctor of Philosophy

In the effort to simulate the biologically inspired continuum robot's dynamic capabilities, researchers have been faced with the daunting task of simulating—in real-time—the complete three dimensional dynamics of the the "beam-like" structure which includes the three "stiff" degrees-of-freedom transverse and dilational shear. Therefore, researchers have traditionally limited the difficulty of the problem with simplifying assumptions. This study, however, puts forward a solution which makes no simplifying assumptions and trades off only the real-time requirement of the desired solution.

The solution is a Finite Difference Time Domain method employing an explicit single step method with cheap right hands sides. The cheap right hand sides are the result of a rather ingenious formulation of the classical beam called the Cosserat rod by, first, the Cosserat brothers and, later, Stuart S. Antman which results in five nonlinear but uncoupled equations that require only multiplication and addition. The method is therefore

suitable for hardware implementation thus moving the real-time requirement from a software solution to a hardware solution.

ACKNOWLEDGMENTS

The author wishes to thank Dr. Younan and Dr. Jones for a casual conversation about nonlinear elasticity which put the three of us together in the pursuit of a numerical solution to the Cosserat rod.

TABLE OF CONTENTS

ACKNOWLEDGMENTS ii

LIST OF FIGURES v

1. INTRODUCTION 1

  1.1 Introduction 1
  1.2 Motivation 2
  1.3 Contributions 3

CHAPTER

2. LITERATURE REVIEW 5

3. METHODOLOGY 7

  3.1 The Cosserat Rod 7
    3.1.1 Kinematics 9
    3.1.2 Mechanics 12
    3.1.3 Constitutive 14
    3.1.4 Partials with Respect to Material Points 16
    3.1.5 Partials with Respect to Time 18
    3.1.6 Antman's System 20
  3.2 Numerical Method 22
    3.2.1 Numerical Stability 24
    3.2.2 Dissipation and Dispersion 26

4. RESULTS 29

  4.1 Validation 29
    4.1.1 Free Fall 30
    4.1.2 Simulated Violin String 31
    4.1.3 Transverse-Dilational Coupling 34
    4.1.4 Transverse-Twist Coupling 36

4.2 Dispersion due to Material Stiffness 36

5. CONCLUSIONS AND FUTURE WORK 39

REFERENCES 41

LIST OF FIGURES

3.1 Director vectors 8

3.2 Cosserat rod 9

3.3 Absolute value of ξ versus p for $\beta = 3140$ 27

3.4 Dissipation versus p for $\beta = 3140$ 27

3.5 Dispersion versus p for $\beta = 3140$ 28

4.1 Stimulation of x axes by induced pluck 32

4.2 Fundamental frequency for simulated “A” string—64N 32

4.3 Fundamental frequency for simulated “A” string—66N 33

4.4 Fundamental frequency for simulated “A” string—65N 33

4.5 Stimulation of y axes by gravity 34

4.6 Distortion of y values by transverse-dilational coupling 35

4.7 Distorsion of x values by transverse-dilational coupling 35

4.8 Distorsion of y values by transverse-twist coupling 36

4.9 Distorsion of x values by transverse-twist coupling 37

4.10 Dispersion due to numerical method 38

4.11 Dispersion due to material stiffness 38

CHAPTER 1

INTRODUCTION

1.1 Introduction

The elephant trunk can pick a single blade of grass and yet move an entire tree. The octopus arm can move rocks in search of prey and then capture that prey with an astonishingly fast prey strike. These biological systems, termed muscular hydroststs [1], thus display an amazing range of dexterity, strength and speed. These creatures depend on the dynamics of their appendages for many essential behaviors, such as the prey strike. Therefore any model useful for the development of realistic continuum robots that emulate the elephant trunk or the octopus arm must be a complete three dimensional (3D) dynamic description.

There are numerous current and proposed applications for continuum robots, as has been ably put forward in a review of the current state of the art by Webster and Jones [2], such as undersea manipulation, toxic area cleanup, assembly line painting, nuclear reactor repair and search and rescue. Other areas of employment are in the medical field for forceps, catheters and steerable needles in robotized surgical systems. Though each of the above applications requires accurate placement and control and would therefore benefit from a more accurate prediction of responses to body forces and tip loadings provided by a complete 3D dynamic model, the undersea manipulation and search and rescue robots, as well as others not yet envisioned, would additionally profit from a highly dynamic capability like the prey strike.

1.2 Motivation

A complete, accurate model for continuum robot dynamics provides many essential capabilities which could enable a new generation of nimble, fast, agile continuum robots. There are many open questions—several of which are discussed below—on the dynamics of continuum robots which cannot be addressed by a static, quasi-static or limited dimensionality model but could be answered by employing an appropriately damped dynamic model.

Material specific damping is key to continued development of biologically inspired continuum robots. A dynamic structure will store energy when stimulated and the appropriately damped dynamic model—unlike the static, quasi-static, undamped or limited dimensionality models—can be used to understand and optimize the intentional utilization of that stored energy in the robot's dynamic structure for such behaviors as grasping and, ultimately, prey strikes.

Elastic structures will, of course, vibrate when forced therefore vibration management will be an essential element of the objective continuum robotics system. Currently robotics systems have to wait until transients damp out before beginning a new motion. With the appropriately damped dynamic model the stimulus-response characteristics can be truly representative of the biological systems we wish to emulate.

Furthermore, an appropriately damped dynamic model allows rapid reactive response dynamic behaviors not possible with current models. Rapid reactive response is necessary to provide for actions such as catching or throwing a ball which includes a number of desired behaviors. Catching a ball requires an awareness of the current environment with ball position and velocity. Additionally, compliance must be controlled to eliminate bounce-off if the “glove” should be too firm. Sensor development must support the environmental awareness, compliance control and other desired capabilities. The appropriately damped dynamic model can support the development and testing of the sensors and algorithms necessary to support these rapid reactive response dynamic behaviors.

In summary, emulating the desired biological behaviors requires an appropriately damped dynamic model as opposed to the models currently available.

1.3 Contributions

Biologically inspired continuum robotics aims to emulate the functionality of both the elephant trunk and octopus arm though they span such an intimidating dynamic range in both strength and speed. Thus continuum robotics researchers find themselves in a dilemma. A realistic model is difficult—if not impossible—to solve in real time. Some researchers have therefore employed constant curvature models based on simplified kinematics which run in real time but evidence significant placement error [2]. Other researchers have employed static models which fail to capture the dynamics inherent in any continuum manipulator. Thus far no researcher has demonstrated a complete 3D dynamic solution. Therefore, the contribution of this study is a solution that is not real-time but is simple enough to be moved toward real-time by massive parallelization (GPU computing) or by implementation in hardware.

The solution is a finite difference time domain implementation. Furthermore, the solution method is reasonably conservative in that no numerical damping other than that inherent in the difference equations has been employed for the base platform; material-specific damping will however be added as future work. Finally, in order to facilitate parallelization or hardware implementation, the method of solution is a single-step explicit method with cheap right hand sides.

The current state of the project is a working model demonstrating all six degrees of freedom. The model is, however, limited to scenarios with both fixed or both free end points due to issues with the calculation of boundary conditions. The model is stable for non-forcing excitation which includes various pulses induced by transitory stimulation.

CHAPTER 2

LITERATURE REVIEW

Continuum robots, as well as the biological appendages that they emulate, are conceptually like beams from classical mechanics; they are continuous 3D dynamic structures with the length much greater than the diameter. Furthermore, though they have infinite degrees of freedom, they have but six degrees of control. Thus classical beam theory provides a framework within which to analyze the complete 3D dynamics of the continuum robot.

We begin with the planar elastica put forth by Euler-Bernoulli. It had the problems of infinite group velocity for longitudinal waves and no shear strains [3]. The group velocity problem was solved by Lord Rayleigh with the inclusion of rotational inertia [3]. Subsequently, Timoshenko included transverse shear strain [3]. We however need a 3D system as opposed to the planar elastica, so we look to Kirchhoff where we gain torque or twist but lose transverse shear strain. Finally we come to the Cosserat brothers followed by Stuart S. Antman [4] who provide a geometrically exact system of equations for a special 3D dynamic beam called a Cosserat rod which has the limitation from a “real” beam in that the cross-section is non-deformable.

Recent approaches which require accurate modeling of the shape of a continuum robot therefore select the Cosserat rod as the best model for the elongated (rod like) continuum robot [5, 6, 7, 2, 8, 9, 10, 11]. Antman's Cosserat rod model provides a system of uncoupled geometrically exact non-linear equations with cheap right hand sides. Thus the Cosserat model—unlike the Euler-Bernoulli or Kirchhoff models—accommodates the three "stiff" degree-of-freedom strains, transverse shear and dilation, as well as the three "soft" degree-of-freedom strains, bending and twisting.

Therefore, the solution for a 3D dynamic model of a continuum robot—which is parameterized both in space (along the beam length) and in time—requires solving a stiff system of non-linear partial differential equations (PDEs) [4]. This is a difficult task [4, 12] and becomes even more difficult if real-time constraints are considered. Therefore, numerous researchers have reduced the degree of difficulty by placing limitations on their model such as restricting motion to a single plane [13, 14, 15], making their models inextensible and quasistatic [16, 8] or even choosing a fully static model [5, 2, 11]. Some researchers have presented the full Cosserat model but provided no information to solve the model [5, 2, 9]. Finally one researcher presents the full Cosserat model [8] and, in another paper [6], provides a significant amount of information on how to solve the proposed system, yet provides only 1D dynamic and 3D quasistatic results.

Though there is a convergence on the Cosserat model, there is no corresponding convergence on a method of solution. The real-time constraint coupled with the Courant-Freidrich-Lewy [1] (CFL) condition [17] likely means there will be no suitable near term method of solution. Therefore, this paper presents a simple yet high fidelity explicit single-step numerical solver that trades off only the real-time aspect of the desired solution.

---

[1] Sampling must occur at a rate faster than the nodal information can change

CHAPTER 3

METHODOLOGY

3.1 The Cosserat Rod

The Cosserat rod is a mathematical construct. Imagine a vanishingly thin filament forming a center-line or space-curve $\mathbf{r}(s, t)$ in global space and then imagine thin cylindrical disks threaded on the filament and constrained to remain undistorted. In the limit as the thickness of these disks approaches zero it becomes the continuous Cosserat rod which retains all of the characteristics of the beam that are of interest to us. However, we no longer have to worry about Poisson expansion, lateral inertia [18] or the probabilistic nature of internal damping [19] as the disks cannot distort, are homogeneous and—for our purpose—identical. We are now free to derive a deterministic geometrically exact nonlinear system of equations describing the three dimensional dynamics of the Cosserat rod.

The Cosserat rod's position and orientation in global space is uniquely defined by the location of each material point s and the orientation of two orthonormal vectors $\mathbf{d}_1$ and $\mathbf{d}_2$ located at these material points. Each $s \in [0, L]$—where 0 is one end of the beam and L is the other—defines the position in global space of a particular "disk" or material point of the rod. The director vectors $\mathbf{d}_1, \mathbf{d}_2$ and $\mathbf{d}_1 \times \mathbf{d}_2 = \mathbf{d}_3$ form an orthonormal basis for the local axes centered at each material point s. Figure 3.1 shows a rod sectioned at an arbitrary material point s with the director vectors $\mathbf{d_1}$ and $\mathbf{d_2}$ constrained to lie in the cross section with $\mathbf{d_3}$ normal to the cross section but not necessarily parallel to the tangent. In fact, the degree to which $\mathbf{d_3}$ is not parallel to the tangent represents the shear deformation.

Since the disks are identical, homogeneous and cannot distort, all that is required to completely describe the disk's position is the location in global space of the disk's center $\mathbf{r}(s, t)$ and the orientation of the director vectors $\mathbf{d}_1(s, t)$ and $\mathbf{d}_2(s, t)$. Figure 3.2 depicts the Cosserat rod—where we show only the center line—we will use for the beam surrogate. We now drop—where appropriate—the spacial and time dependencies for brevity's sake.

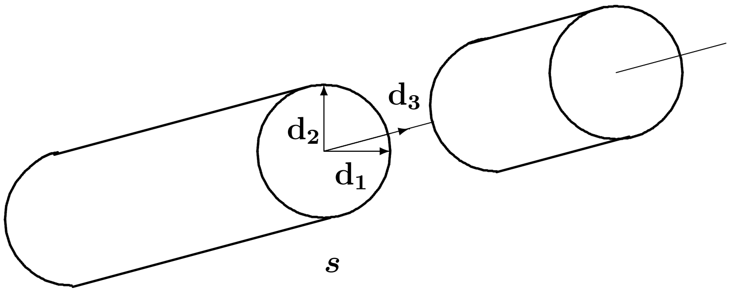

Figure 3.1

Director vectors

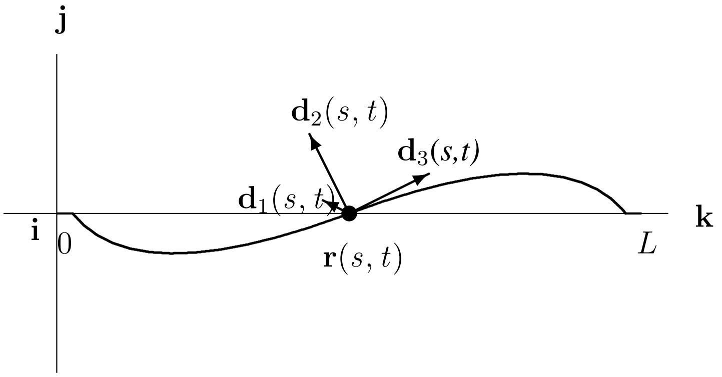

Figure 3.2

Cosserat rod

3.1.1 Kinematics

We restrict our Cosserat rod model to a system wherein stresses cause strains in a linear relationship; therefore Hooke's law is in effect. The two strains that are of interest to us are

$$\boldsymbol{v} = v_k \mathbf{d}_k$$

$$\boldsymbol{u} = u_k \mathbf{d}_k.$$

The repeated subscripts mean that we should sum over the range $1, 2, 3$. We thus have $\boldsymbol{v} = v_1\mathbf{d}_1 + v_2\mathbf{d}_2 + v_3\mathbf{d}_3$ and $\boldsymbol{u} = u_1\mathbf{d}_1 + u_2\mathbf{d}_2 + u_3\mathbf{d}_3$. The strain $\mathbf{v} = [v_1, v_2, v_3]^T$ is the shear triple where v_1 and v_2 are shear strains and v_3 is the dilational strain. The strain $\mathbf{u}$ [1] $= [u_1, u_2, u_3]^T$ is the bending triple where u_1 and u_2 represent bending strains and u_3 represents twisting strain. However knowing current and past values of $\boldsymbol{v}$ and $\boldsymbol{u}$ alone are

---

[1] Global vector variables are in bold symbol font ($\boldsymbol{u}$), local vector variables are in math bold font ($\mathbf{u}$) and scalars—always local—are in math font (u).

of little value; what is needed is the time partials $\boldsymbol{v}_t$ and $\boldsymbol{u}_t$ so that we can calculate future values of $\boldsymbol{v}$ and $\boldsymbol{u}$ given known current and previous vales.

We begin with spatial (with respect to $\boldsymbol{s}$) and time derivatives of the director vectors $\mathbf{d}_k$. From differential geometry [20] we have

$$\begin{aligned} \partial_s \mathbf{d}_k &= \boldsymbol{u} \times \mathbf{d}_k \\ \partial_t \mathbf{d}_k &= \boldsymbol{w} \times \mathbf{d}_k, \end{aligned}$$

where $\boldsymbol{u}$ is the spacial rate of bending and $\boldsymbol{w}$ is the angular velocity of the frame. Furthermore we have

$$\begin{aligned} \partial_s \boldsymbol{r} &= v_k \mathbf{d}_k \\ &= \mathbf{R}\mathbf{v} \end{aligned} \tag{3.1}$$

with

$$\mathbf{R} = \begin{bmatrix} \mathbf{d}_{1i} & \mathbf{d}_{2i} & \mathbf{d}_{3i} \\ \mathbf{d}_{1j} & \mathbf{d}_{2j} & \mathbf{d}_{3j} \\ \mathbf{d}_{1k} & \mathbf{d}_{2k} & \mathbf{d}_{3k} \end{bmatrix}$$

where we see that we cannot just do a simple finite difference to calculate v_k. We would in theory have to solve the linear system $\mathbf{v} = \mathbf{R}^{-1}\partial_s \boldsymbol{r}$ for each node; however, this is not required. We have two options. Since the rotation matrix $\mathbf{R}$ is orthogonal we need do no more than calculate inner products. The other option—following Antman's example—is to make use of compatibility equations, the genesis of which is the requirement that

$$\partial_t \partial_s \boldsymbol{r} = \partial_s \partial_t \boldsymbol{r} \tag{3.2}$$

$$\partial_t \partial_s \mathbf{d}_k = \partial_s \partial_t \mathbf{d}_k. \tag{3.3}$$

We now substitute for $\partial_s \boldsymbol{r}$ and $\partial_t \boldsymbol{r}$ in (3.2) which provides

$$\partial_t(v_k \mathbf{d}_k) \quad = \quad \partial_s(\boldsymbol{r}_t)$$

where we follow Antman and employ $\boldsymbol{p}$ in place of $\boldsymbol{r}_t$. We therefore substitute $\boldsymbol{p}$ for $\boldsymbol{r}_t$ and rearrange to get

$$\begin{aligned}
\boldsymbol{p}_s &= \partial_t(v_k)\mathbf{d}_k + v_k \partial_t \mathbf{d}_k \\
&= \partial_t(v_k)\mathbf{d}_k + v_k(\boldsymbol{w} \times \mathbf{d}_k) \\
&= \boldsymbol{v}_t + \boldsymbol{w} \times v_k \mathbf{d}_k \\
&= \boldsymbol{v}_t + \boldsymbol{w} \times \boldsymbol{v}
\end{aligned}$$

and we have the global expression for the velocity of shearing $\boldsymbol{v}_t$

$$\boldsymbol{v}_t \quad = \quad \boldsymbol{p}_s - \boldsymbol{w} \times \boldsymbol{v}.$$

We must now treat (3.3). We proceed by

$$\begin{aligned}
\partial_t(\boldsymbol{u} \times \mathbf{d}_k) &= \partial_s(\boldsymbol{w} \times \mathbf{d}_k) \\
\boldsymbol{u}_t \times \mathbf{d}_k + \boldsymbol{u} \times \partial_t \mathbf{d}_k &= \boldsymbol{w}_s \times \mathbf{d}_k + \boldsymbol{w} \times \partial_s \mathbf{d}_k \\
(\boldsymbol{u}_t - \boldsymbol{w}_s) \times \mathbf{d}_k &= \boldsymbol{w} \times (\boldsymbol{u} \times \mathbf{d}_k) - \boldsymbol{u} \times (\boldsymbol{w} \times \mathbf{d}_k) \\
&= \boldsymbol{u}(\boldsymbol{w} \cdot \mathbf{d}_k) - (\boldsymbol{w} \cdot \boldsymbol{u})\mathbf{d}_k - \\
&\quad\ \boldsymbol{w}(\boldsymbol{u} \cdot \mathbf{d}_k) + (\boldsymbol{u} \cdot \boldsymbol{w})\mathbf{d}_k \\
&= w_k \boldsymbol{u} - u_k \boldsymbol{w}.
\end{aligned}$$

Given a $\mathbf{d}_j$, $\mathbf{d}_k$ and $\mathbf{d}_j \times \mathbf{d}_k = \mathbf{d}_l$ basis, dotting both sides with $\mathbf{d}_l$ gives

$$\begin{aligned}(\boldsymbol{u}_t - \boldsymbol{w}_s) \times \mathbf{d}_k \cdot \mathbf{d}_l &= w_k \boldsymbol{u} \cdot \mathbf{d}_l - u_k \boldsymbol{w} \cdot \mathbf{d}_l \\ (\boldsymbol{u}_t - \boldsymbol{w}_s) \cdot (\mathbf{d}_k \times \mathbf{d}_l) &= w_k u_l - u_k w_l \\ (\boldsymbol{u}_t - \boldsymbol{w}_s) \cdot \mathbf{d}_j &= (\boldsymbol{w} \times \boldsymbol{u}) \cdot \mathbf{d}_j.\end{aligned}$$

Multiplying both sides by $\mathbf{d}_j$ returns the above scalar equation to the global expression for $\boldsymbol{u}_t$

$$\boldsymbol{u}_t = \boldsymbol{w}_s - \boldsymbol{u} \times \boldsymbol{w}.$$

3.1.2 Mechanics

We now have $\boldsymbol{v}_t$ and $\boldsymbol{u}_t$ but they are in terms of $\boldsymbol{p}$ and $\boldsymbol{w}$; we therefore need the time partials $\boldsymbol{p}_t$ and $\boldsymbol{w}_t$ so that we can calculate future values of $\boldsymbol{p}$ and $\boldsymbol{w}$. What is needed are force and torque balance equations; we look to Antman's derivations in [4]

Antman employs a concept of balancing contact forces at arbitrary material points $\boldsymbol{s}$ and $\boldsymbol{a}$. These contact forces are the shear forces $\boldsymbol{n}$ at points $\boldsymbol{s}$ and $\boldsymbol{a}$ and the body force $\int_a^{\boldsymbol{s}} \boldsymbol{f}(\boldsymbol{s}, t) ds$. He then allows point $\boldsymbol{a}$ to approach point $\boldsymbol{s}$ effectively taking the differential with respect to $\boldsymbol{s}$. Antman's force balance equation is therefore

$$\rho A \int_a^s \boldsymbol{p}_t(\boldsymbol{s}, t) ds = \boldsymbol{n}(\boldsymbol{s}, t) - \boldsymbol{n}(\boldsymbol{a}, t) + \int_a^s \boldsymbol{f}(\boldsymbol{s}, t) ds$$

where we take the partial with respect to $\boldsymbol{s}$ and we have

$$\rho A \boldsymbol{p}_t = \boldsymbol{n}_s + \boldsymbol{f} \tag{3.4}$$

which provides $\boldsymbol{p}_t = \boldsymbol{r}_{tt}$ where ρ is the mass density of the rod and A is the cross sectional area of the rod. The conservative force balance equation therefore equates the force per meter due to translational acceleration $\boldsymbol{r}_{tt}$ to the sum of the partial with respect to $\boldsymbol{s}$ of the shear force $\boldsymbol{n}$ and the distributed body force $\boldsymbol{f}$.

We also require $\boldsymbol{w}_t$ so we need a torque balance equation. Antman provides a torque balance equation which balances the moments over the interval between points $\boldsymbol{s}$ and $\boldsymbol{a}$ caused by the contact forces at $\boldsymbol{s}$ and $\boldsymbol{a}$, the body forces and distributed torques over the interval and the internal moments at $\boldsymbol{s}$ and $\boldsymbol{a}$. As above, Antman allows the point $\boldsymbol{a}$ to approach point $\boldsymbol{s}$. Using the second moment of area tensor for a solid circular rod,

$$\mathbf{J} = \begin{bmatrix} \frac{1}{2}A\kappa^2 & 0 & 0 \\ 0 & \frac{1}{2}A\kappa^2 & 0 \\ 0 & 0 & A\kappa^2 \end{bmatrix}$$

where κ is the radius of gyration [2], we therefore have

$$\begin{aligned} \int_a^s \boldsymbol{r}(\boldsymbol{s},t) \times \rho A \boldsymbol{p}_t(\boldsymbol{s},t) ds \quad + \quad & \int_a^s \rho \mathbf{J} \boldsymbol{w}_t(\boldsymbol{s},t) ds = \boldsymbol{m}(\boldsymbol{s},t) - \boldsymbol{m}(\boldsymbol{a},t) + \boldsymbol{r}(\boldsymbol{s},t) \times \boldsymbol{n}(\boldsymbol{s},t) \\ & -\boldsymbol{r}(\boldsymbol{a},t) \times \boldsymbol{n}(\boldsymbol{a},t) + \int_a^s \left(\boldsymbol{r}(\boldsymbol{s},t) \times \boldsymbol{f}(\boldsymbol{s},t) + \boldsymbol{l}(\boldsymbol{s},t)\right) ds \end{aligned}$$

where we substitute (3.4) in for $\boldsymbol{p}_t$ which gives

$$\rho \mathbf{J} \boldsymbol{w}_t \quad = \quad \boldsymbol{m}_s + \boldsymbol{r}_s \times \boldsymbol{n} + \boldsymbol{l} \qquad (3.5)$$

for the conservative torque balance equation, for the circular rod, when the partial with respect to s is taken of both sides. $\boldsymbol{m}$ is the bending moment, $\boldsymbol{r}_s \times \boldsymbol{n}$ is the cross product of the shear deformation and the shear force and $\boldsymbol{l}$ is the distributed body torque.

---

[2] The radius of gyration $\kappa = \frac{R}{\sqrt{2}}$ where R is the radius of the circular rod.

Taking inventory we have

$$
\begin{aligned}
\boldsymbol{v}_t &= \boldsymbol{p}_s - \boldsymbol{w} \times \boldsymbol{v} && (3.6) \\
\boldsymbol{p}_t &= (\rho A)^{-1} \left[\boldsymbol{n}_s + \boldsymbol{f} \right] && (3.7) \\
\boldsymbol{w}_t &= (\rho \mathbf{J})^{-1} \left[\boldsymbol{m}_s + \boldsymbol{r}_s \times \boldsymbol{n} + \boldsymbol{l} \right] && (3.8) \\
\boldsymbol{u}_t &= \boldsymbol{w}_s - \boldsymbol{u} \times \boldsymbol{w} && (3.9)
\end{aligned}
$$

which provides a system of four equations with a time derivative on the left hand side and a spacial derivative on the right hand side [12]. The fifth and final equation $(\mathbf{d}_k)_t = \boldsymbol{w} \times \mathbf{d}_k$ is of course solved directly. The important point is that everything on the right hand sides is known and the left hand sides provide future values thus marching the solution forward in time. Therefore we have a system of five uncoupled nonlinear equations which can be solved numerically using the finite difference time domain method.

3.1.3 Constitutive

It has been established that $\boldsymbol{n}$ and $\boldsymbol{m}$ are the shear force and bending moments respectively but we have not demonstrated how a magnitude is determined. Herein we develop the material dependent relationship between the shear strain $\boldsymbol{v}$ and the shear force $\boldsymbol{n}$ and the relationship between the bending strain $\boldsymbol{u}$ and the bending moment $\boldsymbol{m}$.

The shear modulus G is the measure of the material's resistance to shear. The modulus of elasticity E is the measure of the material's resistance to dilation. These moduli are measured in Newtons per square meter. We therefore have, since we have invoked Hooke's law, for the shear force $\boldsymbol{n}$

$$\boldsymbol{n} \;=\; \mathbf{D}\boldsymbol{v} - D_{33}\mathbf{d}_3 \tag{3.10}$$

where $\mathbf{D}$ is

$$\mathbf{D} \;=\; \begin{bmatrix} GA & 0 & 0 \\ 0 & GA & 0 \\ 0 & 0 & EA \end{bmatrix}.$$

It is important to note that the initial undisturbed value for $\mathbf{v}$ is $[0, 0, 1]^T$. If v_3 is greater than 1 the material is said to be stretched and if v_3 is less than 1 the material is said to be compressed.

For the bending moment $\boldsymbol{m}$ we have

$$\boldsymbol{m} \;=\; \mathbf{C}\boldsymbol{u}, \tag{3.11}$$

where $\mathbf{C}$ is

$$\mathbf{C} \;=\; \begin{bmatrix} EA\kappa^2 & 0 & 0 \\ 0 & EA\kappa^2 & 0 \\ 0 & 0 & GA\kappa^2 \end{bmatrix}$$

and κ is the shape dependent radius of gyration measured in meters. Equations 3.10 and 3.11 show the linear (Hooke's law) relationship we alluded to earlier as G, E, A, and κ are constants.

3.1.4 Partials with Respect to Material Points

We must now address the issue of spacial partials with respect to $\boldsymbol{s}$. We need—in order to compute the right hand sides—to take the partials with respect to the material points $\boldsymbol{s}$ of $\boldsymbol{n}(\boldsymbol{s},t)$, $\boldsymbol{m}(\boldsymbol{s},t)$, $\boldsymbol{p}(\boldsymbol{s},t)$ and $\boldsymbol{w}(\boldsymbol{s},t)$.

We begin with $\boldsymbol{n}(\boldsymbol{s},t)$ and we have

$$\begin{aligned}
\partial_s \boldsymbol{n} &= \partial_s(D_{kk} v_k \mathbf{d}_k - D_{33}\mathbf{d}_3) \\
&= D_{kk}(\partial_s v_k)\mathbf{d}_k + v_k D_{kk}(\boldsymbol{u} \times \mathbf{d}_k) - D_{33}(\boldsymbol{u} \times \mathbf{d}_3) \\
&= \mathbf{D}\boldsymbol{v}_s + \boldsymbol{u} \times \mathbf{D}\boldsymbol{v} - D_{33}(u_2\mathbf{d}_1 - u_1\mathbf{d}_2) \\
&= (\mathbf{D}\mathbf{v}_s + \mathbf{u} \times \mathbf{D}\mathbf{v} - \mathbf{H}\mathbf{u}) \cdot \mathbf{d}_k
\end{aligned}$$

where $\mathbf{H}$ is

$$\mathbf{H} = \begin{bmatrix} 0 & D_{33} & 0 \\ -D_{33} & 0 & 0 \\ 0 & 0 & 0 \end{bmatrix}$$

and therefore the local gradient of shear force is

$$\mathbf{n}_s = \mathbf{D}\mathbf{v}_s + \mathbf{u} \times \mathbf{D}\mathbf{v} - \mathbf{H}\mathbf{u}. \tag{3.12}$$

and the local gradient of shear deformation is

$$\mathbf{v}_s(\boldsymbol{s}) \approx \frac{\mathbf{v}(\boldsymbol{s} + ds) - \mathbf{v}(\boldsymbol{s} - ds)}{2ds}.$$

Note that the local value or triple of $\boldsymbol{v}$ is denoted as $\mathbf{v}$. We will treat the remaining global variables in the same manner.

Therefore $\boldsymbol{m}_s$ is

$$\begin{aligned}
\partial_s \boldsymbol{m} &= \partial_s (C_{kk} u_k \mathbf{d}_k) \\
&= C_{kk}(\partial_s u_k)\mathbf{d}_k + u_k C_{kk}(\boldsymbol{u} \times \mathbf{d}_k) \\
&= C_{kk}(\partial_s u_k)\mathbf{d}_k + \boldsymbol{u} \times \mathbf{C}\boldsymbol{u} \\
&= (\mathbf{C}\mathbf{u}_s + \mathbf{u} \times \mathbf{C}\mathbf{u}) \cdot \mathbf{d}_k.
\end{aligned}$$

The local gradient of the bending moment is therefore

$$\mathbf{m}_s = \mathbf{C}\mathbf{u}_s + \mathbf{u} \times \mathbf{C}\mathbf{u}$$

and

$$\mathbf{u}_s(\boldsymbol{s}) \approx \frac{\mathbf{u}(\boldsymbol{s} + ds) - \mathbf{u}(\boldsymbol{s} - ds)}{2ds}.$$

We have for $\boldsymbol{p}_s$

$$\begin{aligned}
\partial_s \boldsymbol{p} &= \partial_s (p_k \mathbf{d}_k) \\
&= (\partial_s p_k)\mathbf{d}_k + p_k(\boldsymbol{u} \times \mathbf{d}_k) \\
&= (\partial_s p_k)\mathbf{d}_k + \boldsymbol{u} \times \boldsymbol{p} \\
&= (\mathbf{p}_s + \mathbf{u} \times \mathbf{p}) \cdot \mathbf{d}_k \qquad (3.13)
\end{aligned}$$

and of course

$$\mathbf{p}_s(\boldsymbol{s}) \approx \frac{\mathbf{p}(\boldsymbol{s} + ds) - \mathbf{p}(\boldsymbol{s} - ds)}{2ds}.$$

Finally we have

$$
\begin{aligned}
\partial_s \boldsymbol{w} &= \partial_s(w_k \mathbf{d}_k) \\
&= (\partial_s w_k)\mathbf{d}_k + w_k(\boldsymbol{u} \times \mathbf{d}_k) \\
&= (\partial_s w_k)\mathbf{d}_k + \boldsymbol{u} \times \boldsymbol{w} \\
&= (\mathbf{w}_s + \mathbf{u} \times \mathbf{w}) \cdot \mathbf{d}_k
\end{aligned}
\tag{3.14}
$$

where

$$
\mathbf{w}_s(\boldsymbol{s}) \approx \frac{\mathbf{w}(\boldsymbol{s}+ds) - \mathbf{w}(\boldsymbol{s}-ds)}{2ds}.
$$

3.1.5 Partials with Respect to Time

The global spacial partials have been presented in terms of local variables. We must now provide the global time partials $\boldsymbol{v}_t$, $\boldsymbol{p}_t$, $\boldsymbol{w}_t$ and $\boldsymbol{u}_t$ in terms of local variables.

Treating $\boldsymbol{v}_t$ we have

$$
\begin{aligned}
\boldsymbol{v}_t &= \partial_t(v_k \mathbf{d}_k) \\
&= (\partial_t v_k)\mathbf{d}_k + v_k(\boldsymbol{w} \times \mathbf{d}_k) \\
&= (\partial_t v_k)\mathbf{d}_k + \boldsymbol{w} \times \boldsymbol{v} \\
&= (\mathbf{v}_t + \mathbf{w} \times \mathbf{v}) \cdot \mathbf{d}_k
\end{aligned}
\tag{3.15}
$$

where

$$
\mathbf{v}_t(t) \approx \frac{\mathbf{v}(t+dt) - \mathbf{v}(t-dt)}{2dt}.
$$

Next we treat $\boldsymbol{p}_t$

$$\begin{aligned}
\boldsymbol{p}_t &= \partial_t(p_k\mathbf{d}_k) \\
&= (\partial_t p_k)\mathbf{d}_k + p_k(\boldsymbol{w} \times \mathbf{d}_k) \\
&= (\partial_t p_k)\mathbf{d}_k + \boldsymbol{w} \times \boldsymbol{p} \\
&= (\mathbf{p}_t + \mathbf{w} \times \mathbf{p}) \cdot \mathbf{d}_k \qquad (3.16)
\end{aligned}$$

where

$$\mathbf{p}_t(t) \approx \frac{\mathbf{p}(t+dt) - \mathbf{p}(t-dt)}{2dt}.$$

In order to treat $\boldsymbol{w}_t$ we employ a dummy matrix $\mathbf{K} = (\rho\mathbf{J})^{-\mathbf{1}}$ to avoid the $\boldsymbol{w} \times \boldsymbol{w}$ condition and therefore $\boldsymbol{w}_t$ is

$$\begin{aligned}
\boldsymbol{w}_t &= K_{kk}\partial_t(w_k\mathbf{d}_k) \\
&= K_{kk}(\partial_t w_k)\mathbf{d}_k + w_k K_{kk}(\boldsymbol{w} \times \mathbf{d}_k) \\
&= K_{kk}(\partial_t w_k)\mathbf{d}_k + \boldsymbol{w} \times \mathbf{K}\boldsymbol{w} \\
&= (\mathbf{K}\mathbf{w}_t + \mathbf{w} \times \mathbf{K}\mathbf{w}) \cdot \mathbf{d}_k \qquad (3.17)
\end{aligned}$$

where

$$\mathbf{w}_t(t) \approx \frac{\mathbf{w}(t+dt) - \mathbf{w}(t-dt)}{2dt}.$$

Finally

$$\begin{aligned} \boldsymbol{u}_t &= \partial_t(u_k \mathbf{d}_k) \\ &= (\partial_t u_k)\mathbf{d}_k + u_k(\boldsymbol{w} \times \mathbf{d}_k) \\ &= (\partial_t u_k)\mathbf{d}_k + \boldsymbol{w} \times \boldsymbol{u} \\ &= (\mathbf{u}_t + \mathbf{w} \times \mathbf{u}) \cdot \mathbf{d}_k \end{aligned} \tag{3.18}$$

where

$$\mathbf{u}_t(t) \approx \frac{\mathbf{u}(t+dt) - \mathbf{u}(t-dt)}{2dt}.$$

3.1.6 Antman's System

We are now ready to form the system of equations that we will actually solve. The following equations are in terms of local variables. We begin with $\mathbf{v}_t$ where, from equations 3.13 and 3.15, we have

$$\begin{aligned} \mathbf{v}_t + \mathbf{w} \times \mathbf{v} &= \mathbf{p}_s + \mathbf{u} \times \mathbf{p} \\ \mathbf{v}_t &= \mathbf{p}_s + \mathbf{u} \times \mathbf{p} - \mathbf{w} \times \mathbf{v} \end{aligned}$$

which provides the velocity of shearing from which we calculate future vales of shear.

Next we tackle the translational acceleration $\mathbf{p}_t$ where, from equations 3.7 and 3.16, we have

$$\begin{aligned} \rho A(\mathbf{p}_t + \mathbf{w} \times \mathbf{p}) &= \mathbf{n}_s + \mathbf{f} \\ \rho A\mathbf{p}_t + \mathbf{w} \times \rho A\mathbf{p} &= \mathbf{n}_s + \mathbf{f} \\ \mathbf{p}_t &= (\rho A)^{-1}\left[\mathbf{n}_s + \mathbf{f} - \mathbf{w} \times \rho A\mathbf{p}\right]. \end{aligned}$$

Given the current translational acceleration and current and past values of $\boldsymbol{r}$ we can calculate future values for $\boldsymbol{r}$ by

$$\begin{aligned}\mathbf{p}_t \cdot \mathbf{d}_k &\approx \frac{\boldsymbol{r}(t+dt) - 2\boldsymbol{r}(t) + \boldsymbol{r}(t-dt)}{dt^2} \\ \boldsymbol{r}(t+dt) &\approx dt^2 \mathbf{p}_t \cdot \mathbf{d}_k + 2\boldsymbol{r}(t) - \boldsymbol{r}(t-dt).\end{aligned}$$

The torque balance equation provides the angular acceleration $\mathbf{w}_t$ which is given by, from equations 3.8 and 3.17,

$$\begin{aligned}\rho \mathbf{J} \mathbf{w}_t - \mathbf{w} \times \rho \mathbf{J} \mathbf{w} &= \mathbf{m}_s + \mathbf{v} \times \mathbf{n} + \mathbf{l} \\ \mathbf{w}_t &= (\rho \mathbf{J})^{-1} \left[\mathbf{m}_s + \mathbf{v} \times \mathbf{n} + \mathbf{l} - \mathbf{w} \times \rho \mathbf{J} \mathbf{w} \right]\end{aligned}$$

where $\mathbf{n}$ is the local value of the shear force. It provides future values of the angular velocity $\boldsymbol{w}$.

The velocity of bending strain $\mathbf{u}_t$ is, from equations 3.14 and 3.18,

$$\begin{aligned}\mathbf{u}_t + \mathbf{w} \times \mathbf{u} &= \mathbf{w}_s + \mathbf{u} \times \mathbf{w} - \mathbf{u} \times \mathbf{w} \\ \mathbf{u}_t &= \mathbf{w}_s - \mathbf{w} \times \mathbf{u}\end{aligned}$$

which provides future values for the bending strain $\boldsymbol{u}$.

Finally we need future values of $\mathbf{d}_k$. The global finite difference equation

$$\begin{aligned}\partial_t \mathbf{d}_k &= \boldsymbol{w} \times \mathbf{d}_k \\ \frac{\mathbf{d}_k(t+dt) - \mathbf{d}_k(t-dt)}{2dt} &\approx \boldsymbol{w} \times \mathbf{d}_k \\ \mathbf{d}_k(t+dt) &\approx 2dt(\boldsymbol{w} \times \mathbf{d}_k) + \mathbf{d}_k(t-dt)\end{aligned}$$

provides them. We are now ready to solve Antman's system but we need a conservative yet stable method for doing so.

3.2 Numerical Method

The proposed system is composed of the force and torque balance equations and three auxiliary equations. The mesh ratio [3] p is nominally equal to $\frac{1}{\beta}$ where $\beta = \sqrt{E/\rho}$ is the maximum phase velocity and $\frac{1}{\beta}$ is the CFL condition on the mesh ratio. However $p :\rightarrow p(h = \Delta x)$ is the experimentally determined largest stable multiplier for the fully coupled condition where all the modes are stimulated simultaneously. The spacial step size h is of course variable but should be set at some fraction of the beam's diameter. The mesh ratio p and the spacial step size h therefore determine the time step size k.

We begin with the force balance system, (3.4),

$$\rho A \frac{(\mathbf{p}_m^{n+1} - \mathbf{p}_m^{n-1})}{2k} = \mathbf{n}_s + \mathbf{f} - \mathbf{w} \times \rho A \mathbf{p}$$

$$\begin{aligned} \mathbf{n}_s = {} & [GAv_{1_s}\mathbf{d}_1 + GAv_{2_s}\mathbf{d}_2 + EAv_{3_s}\mathbf{d}_3 + \\ & GAv_1(\mathbf{u} \times \mathbf{d}_1) + GAv_2(\mathbf{u} \times \mathbf{d}_2) + \\ & EA(v_3 - 1)(\mathbf{u} \times \mathbf{d}_3)] \cdot [\mathbf{d}_1 + \mathbf{d}_2 + \mathbf{d}_3] \end{aligned}$$

$$\begin{aligned} v_{k_s} &\approx \frac{(v^n_{k_{m+1}} - v^n_{k_{m-1}})}{2h} \\ \mathbf{u} \times \mathbf{d}_k &= [u_1\mathbf{d}_1 + u_2\mathbf{d}_2 + u_3\mathbf{d}_3] \times \mathbf{d}_k \\ \mathbf{f} &= [F_i\mathbf{i} + (F_j - F_g)\mathbf{j} + F_k\mathbf{k}] \cdot \\ & \quad [\mathbf{d}_1 + \mathbf{d}_2 + \mathbf{d}_3] \end{aligned}$$

---

[3] The mesh ratio p is the time step $k = \Delta t$ divided by the spacial step $h = \Delta x$.

where the object is to solve for $\boldsymbol{p}^{n+1}$—the future value—given the current and past values $(\cdot)^n$,$(\cdot)^{n-1}$ for all M nodes. $F_{i,j,k}$ are externally applied global distributed shear forces and F_g is the global distributed force due to gravity. Any variable with no superscript designating a time sequence is a current value and any variable without a subscript designating a nodal sequence is the current node.

The torque balance system, (3.5), is

$$\begin{aligned}
\rho\mathbf{J}\left(\frac{\mathbf{w}_m^{n+1}-\mathbf{w}_m^{n-1}}{2k}\right) &= \mathbf{m}_s+\mathbf{r}_s\times\mathbf{n}+\mathbf{l}-\mathbf{w}\times\rho\mathbf{J}\mathbf{w} \\
\mathbf{m}_s &= [EJ_{1,1}u_{1s}\mathbf{d}_1+EJ_{2,2}u_{2s}\mathbf{d}_2+ \\
&\quad EJ_{3,3}u_{3s}\mathbf{d}_3+EJ_{1,1}u_1(\mathbf{u}\times\mathbf{d}_1)+ \\
&\quad EJ_{2,2}u_2(\mathbf{u}\times\mathbf{d}_2)+EJ_{3,3}u_3(\mathbf{u}\times\mathbf{d}_3)]\cdot[\mathbf{d}_1+\mathbf{d}_2+\mathbf{d}_3]
\end{aligned}$$

$$\begin{aligned}
u_{k_s} &\approx \frac{(u_{k_{m+1}}^n-u_{k_{m-1}}^n)}{2h} \\
\mathbf{l} &= [T_i\mathbf{i}+T_j\mathbf{j}+T_k\mathbf{k}]\cdot[\mathbf{d}_1+\mathbf{d}_2+\mathbf{d}_3]
\end{aligned}$$

where the $T_{i,j,k}$ are externally applied distributed torques.

The three auxiliary equations are

$$\begin{aligned}
\frac{(\mathbf{u}_m^{n+1}-\mathbf{u}_m^{n-1})}{2k} &= \frac{(\mathbf{w}_{m+1}^n-\mathbf{w}_{m-1}^n)}{2h}-\mathbf{w}_m^n\times\mathbf{u}_m^n \\
\frac{(\mathbf{v}_m^{n+1}-\mathbf{v}_m^{n-1})}{2k} &= \frac{(\mathbf{p}_{m+1}^n-\mathbf{p}_{m-1}^n)}{2h}+\mathbf{u}_m^n\times\mathbf{p}_m^n-\mathbf{w}_m^n\times\mathbf{v}_m^n \\
\frac{(\mathbf{d}_{k_m}^{\ n+1}-\mathbf{d}_{k_m}^{\ n-1})}{2k} &= \mathbf{w}_m^n\times\mathbf{d}_{k_m}^{\ n}.
\end{aligned} \tag{3.19}$$

Here, however, we break with Antman and forgo (3.19) in favor of the global partial with respect to s of $\boldsymbol{r}(\boldsymbol{s},t)$ and solve for the local values of shear via the inner-products

$$\mathbf{v}^{n+1} = \left[\mathbf{R}^{n+1}\right]^T \partial_s \boldsymbol{r}^{n+1}.$$

This alternative has the advantage of providing relief from certain difficulties with boundary conditions on $\boldsymbol{v}_t$.

3.2.1 Numerical Stability

Antman's system is nonlinear and therefore we cannot do a definitive stability analysis. However, the dilation only mode is linear and therefore amenable to analysis. We begin with (3.4)

$$\rho A \boldsymbol{p}_t = \boldsymbol{n}_s + \boldsymbol{f}$$

which we convert to a scalar equation based on the dilation only assumption. We now have

$$\rho A p_t = n_s \tag{3.20}$$

where the dependencies and external forces have been dropped. In order to do a stability analysis we must first rewrite (3.20) as a left side time derivative and a right side space derivative of the same variable. Rewriting (3.20) using (3.12) gives

$$\begin{aligned} \rho A r_{tt} &= (\mathbf{D}\mathbf{v}_s + \mathbf{u} \times \mathbf{D}\mathbf{v} - \mathbf{H}\mathbf{u}) \cdot \mathbf{d}_3 \\ &= EAv_s. \end{aligned}$$

where, since there are no bending strains, the terms in $\mathbf{u}$ drop out. Using (3.1) we have

$$\begin{aligned}\rho A r_{tt} &= EAv_s \\ r_{tt} &= \beta^2 \partial_s(\mathbf{R}^T \boldsymbol{r}_s) \cdot \mathbf{d}_3 \\ &= \beta^2(\partial_s \mathbf{R}^T \boldsymbol{r}_s + \mathbf{R}^T \boldsymbol{r}_{ss}) \cdot \mathbf{d}_3\end{aligned}$$

and since there are no bending strains the $\partial_s \mathbf{R}^T$ term drops out leaving

$$\begin{aligned}r_{tt} &= \beta^2(\mathbf{R}^T \boldsymbol{r}_{ss}) \cdot \mathbf{d}_3 \\ &= \beta^2 \alpha r_{ss}\end{aligned}$$

where αr_{ss} is the local $\mathbf{d}_3$ component of the global $\boldsymbol{r}_{ss}$. Aligning $\mathbf{d}_3$ with the $\mathbf{k}$ axis we have

$$r_{tt} = \beta^2 r_{ss}.$$

Using the following discretization

$$\begin{aligned}&\frac{(r_{n+1,m} - 2r_{n,m} + r_{n-1,m})}{k^2} - \frac{\beta^2}{h^2}\left(\frac{1}{90}(r_{n,m+3} + r_{n,m-3}) - \frac{3}{20}(r_{n,m+2} + r_{n,m-2}) + \right. \\ &\left. \frac{3}{2}(r_{n,m+1} + r_{n,m-1}) - \frac{49}{18} r_{n,m}\right) = 0 \\ &r_{n+1,m} - 2r_{n,m} + r_{n-1,m} - p^2\beta^2\left(\frac{1}{90}(r_{n,m+3} + r_{n,m-3}) - \frac{3}{20}(r_{n,m+2} + r_{n,m-2}) + \right. \\ &\left. \frac{3}{2}(r_{n,m+1} + r_{n,m-1}) - \frac{49}{18} r_{n,m}\right) = 0 \qquad (3.21)\end{aligned}$$

which is $O(h^6)$ and the Von Neumann stability method where $r_{n\pm i,m\pm j}$ is represented as $\exp(\alpha(n \pm i)k) exp(I(m \pm j)\beta h)$ we substitute into (3.21) and solve for the gain factor ξ where $\xi = \exp(\alpha k)$. We next solve for the mesh ratio p where $|\xi| = 1$. This gives

$$p = \frac{3}{34}\sqrt{85}\frac{1}{\beta}$$

for the maximum stable mesh ratio for the dilation only mode. The fully stimulated modes, however, require a smaller, experimentally determined, mesh ratio.

3.2.2 Dissipation and Dispersion

The numerical method of choice will, unfortunately, cause non-objective or numerical dissipation and dispersion as a side effect. The important consideration is that the undesired dissipation and dispersion be significantly less than the objective dissipation and dispersion. We, unfortunately, cannot determine the ratio of numerical to objective dissipation and dispersion without implementing material specific damping. Nevertheless, we can check to see if the numerical dissipation and dispersion are small.

Since we have an expression for ξ from § 3.2.1 above we can break the system response into its real part, dissipation, and its imaginary part, dispersion. We first pick the worst case value for β where $\cos(\beta h) = -1$ which we then use for plotting $|\xi|$, $\Re(\xi)$ and $\Im(\xi)$ versus p.

Though, as we see from Figure 3.3, the absolute value of p is very close to one, Figures 3.4 and 3.5 show that there is a small amount of dissipation and dispersion. It should be noted that this is the best case—dilation only—scenario. For the general case the dissipation and dispersion are unknown but likely to be worse. Until material specific damping is included in the model no true evaluation of numerical versus objective dissipation and dispersion is possible.

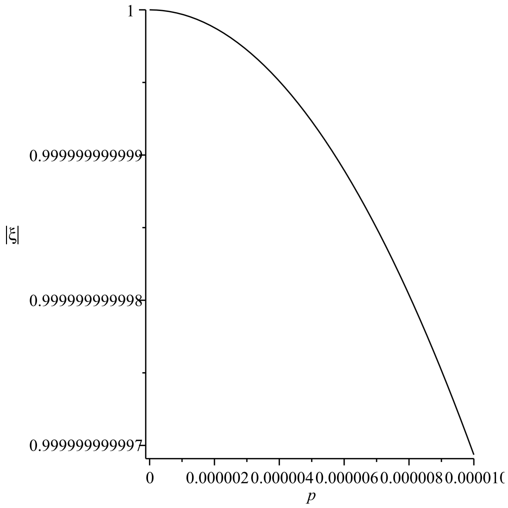

Figure 3.3

Absolute value of ξ versus p for $\beta = 3140$

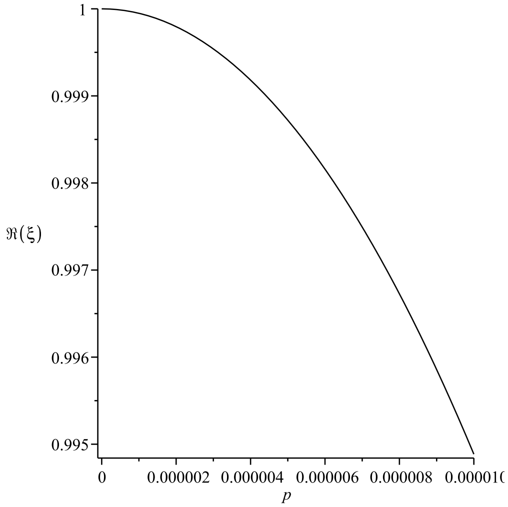

Figure 3.4

Dissipation versus p for $\beta = 3140$

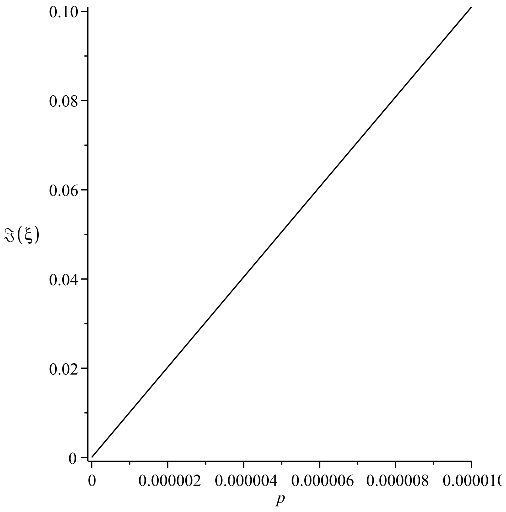

Figure 3.5

Dispersion versus p for $\beta = 3140$

CHAPTER 4

RESULTS

The usual way to simulate a dynamic beam with any aspiration towards real time is to avoid one or all of the three stiff degree of freedom modes. The one most often avoided is the dilational mode which usually ($E > G$) has the most impact on the CFL condition. What is lost when the stiff degree of freedom modes are sacrificed is mode coupling. The two transverse modes—the usual modes of interest—couple through both the dilational mode and the twist mode. It is imperative therefor that a complete 3D dynamic simulation demonstrate these couplings as well as the traditional dynamic behaviors a beam is heir to.

The Antman system—with the noted exception for $\mathbf{v}_t$—presented in $\S$ 3.1.6 has been coded in C. This system, fully stimulated, has proved to be stable (double precision) over a one second interval which is sufficient for our immediate purposes. It should be noted however, that this system is conservative as there is no material dependent or numerical damping applied; it is, therefore, expected to be unstable [4, 12]. This considered, the following stimulations will be limited to those that do not trigger this inherent instability.

4.1 Validation

There are three basic boundary condition scenarios for a rod or cable:

1. Free fall (free end-free end),
2. Cantilever(fixed end-free end),

3. Catenary (fixed end-fixed end).

Though it is desirable to demonstrate a close match between these scenarios and empirical data we can only match the free fall (vacuum) scenario with the theoretical acceleration of gravity. Comparing the behaviors of scenarios 2 and 3 with empirical data requires system specific damping which is out of scope for this effort.

We can, however, compare the fundamental phase velocity for scenario 3 as it is consistent with the fundamental phase velocity—thus frequency—of a musical instrument string such as the "A" string of the violin. Simulating the appropriate string parameters, the appropriate active length and the appropriate tension should produce a pulse with the fundamental frequency of 440 Hertz (Hz). We therefore simulate the violin "A" string and present the results below. Furthermore, we present examples of mode coupling and material specific dispersion.

The following demonstrations are for a thin steel wire (violin "A" string) with a relatively high Young's modulus lying (free fall) or stretched (violin string) along the z axes between rigid end supports. The y axis represents the vertical and the x axis represents the horizontal.

4.1.1 Free Fall

A simulation of free fall—scenario 1 above—results in the expected rigid body translation in the yz plane in the negative y direction. After $N = 31$ iterations the bar, initially located at $y = 0$, had translated to $y = -y_n$. The time delta for N iterations is $\delta_t = N/f_s$ seconds where $f_s = 44100$ is the sampling frequency. We therefore have for δ_t

$$\delta_t = \frac{31}{44100} seconds$$

and the percent error e is

$$\begin{aligned} e &= 100\frac{g\frac{\delta_t^2}{2} - y_n}{y_n} \\ &= 0.0043\% \end{aligned}$$

where g is assigned the value 9.80669 meters per second per second.

4.1.2 Simulated Violin String

The nominal tension for a violin “A” string composed of a steel core with aluminium wrapping and an active length of 0.328 meters(M) is 14.1 pounds force (lbf) [21]. Though we are not simulating a steel core aluminium wrapped string, it is the only violin “A” string we have tension data for. However, there is tension data [21] for the “E” string for both the solid steel and the aluminium wrapped steel core strings and, from this data, we learn that there is a $+0.5$ lbf adjustment for the solid steel string. Therefore, the nominal string tension for the solid steel “A” string is 14.6 lbf or 65 Newtons (N).

The following simulation results are for a solid steel violin “A” string with a 0.328M active length for three tension cases centered about 65N. The stimulation is a transient pluck as seen in Figure 4.1. Figure 4.2 shows the case of 64N and shows that the spectral peak lies just below 440Hz. Next, Figure 4.3 is for 66N and shows the spectral peak just above 440Hz. Finally, Figure 4.4 is for 65N and shows the spectral peak is now centered

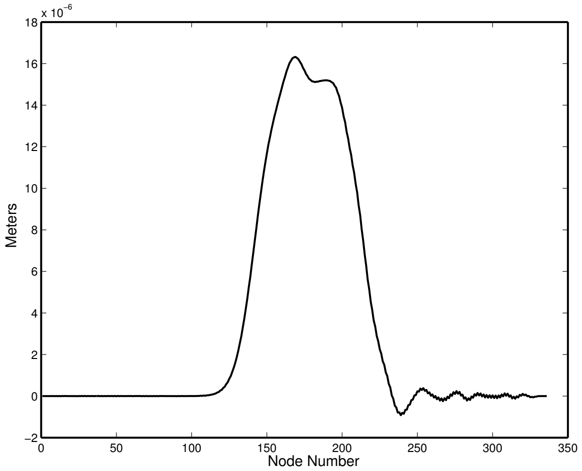

Figure 4.1

Stimulation of x axes by induced pluck

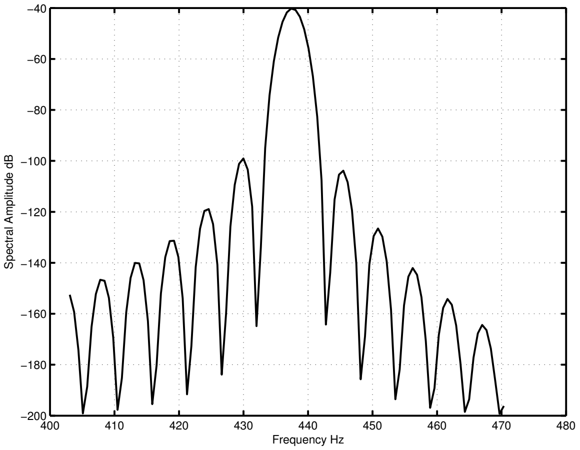

Figure 4.2

Fundamental frequency for simulated “A” string—64N

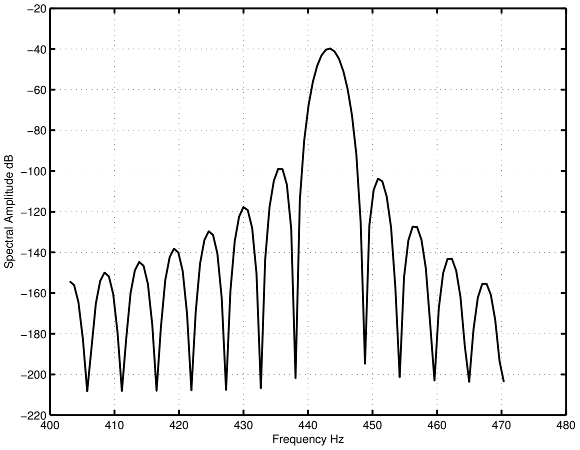

Figure 4.3

Fundamental frequency for simulated “A” string—66N

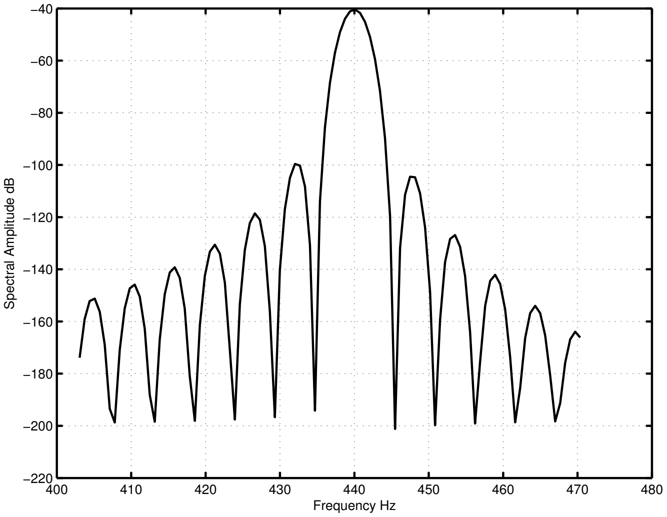

Figure 4.4

Fundamental frequency for simulated “A” string—65N at 440Hz thus verifying the fundamental phase velocity of the simulated string.

4.1.3 Transverse-Dilational Coupling

In order to demonstrate transverse-dilational coupling we stimulate both transverse modes and note the cross disturbance that occurs as a result. Figures 4.5 and 4.1 show the effect of gravity on the y axis and an induced pulse on the x axis respectively.

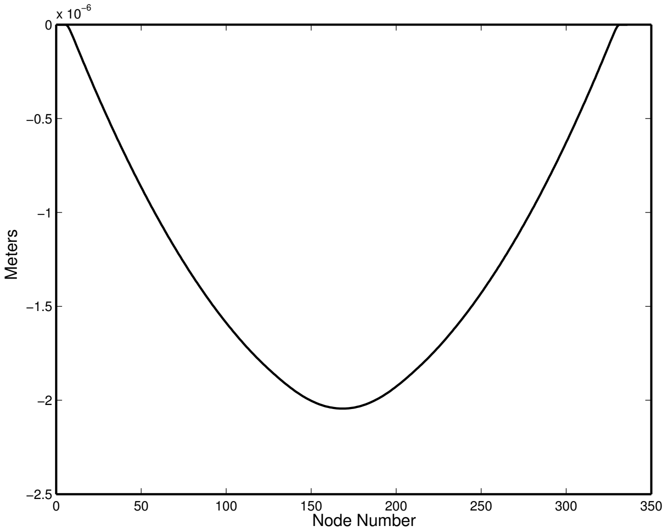

Figure 4.5

Stimulation of y axes by gravity

Figure 4.6 shows the resultant distortions that appear on the y axis due to the pulse on the x axis and the transverse-dilational coupling. Figure 4.7 shows the effect on the x axis due to the same coupling and gravity acting on the y axis. In order to see these distortions the axes values are calculated as the difference between the axis value with and without the other axis being stimulated.

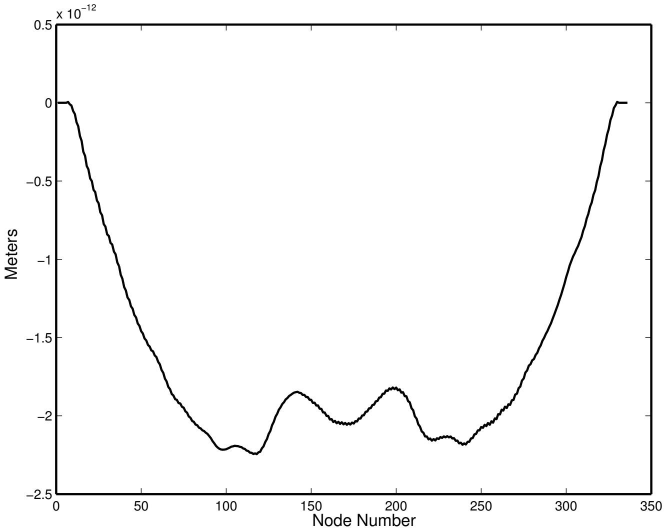

Figure 4.6

Distortion of y values by transverse-dilational coupling

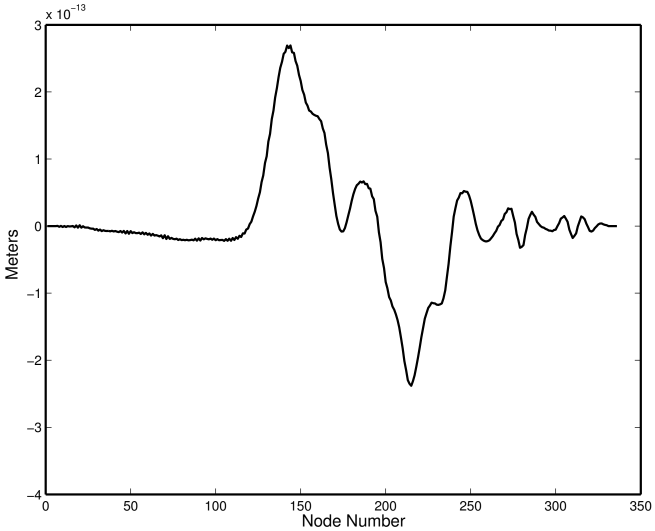

Figure 4.7

Distorsion of x values by transverse-dilational coupling

4.1.4 Transverse-Twist Coupling

The procedure for transverse-twist coupling is the same as above for transverse-dilational coupling except that the dilational shear has to be switched off during the simulation in order to see the transverse-twist coupling. The stimulus to each axis is the same as above.

Figure 4.8 shows the distortions on the y axis due to the x axis pulse and the transverse-twist coupling. Figure 4.9 shows the distortions on the x axis due to the gravitational loading of the y axis and the transverse-twist coupling.

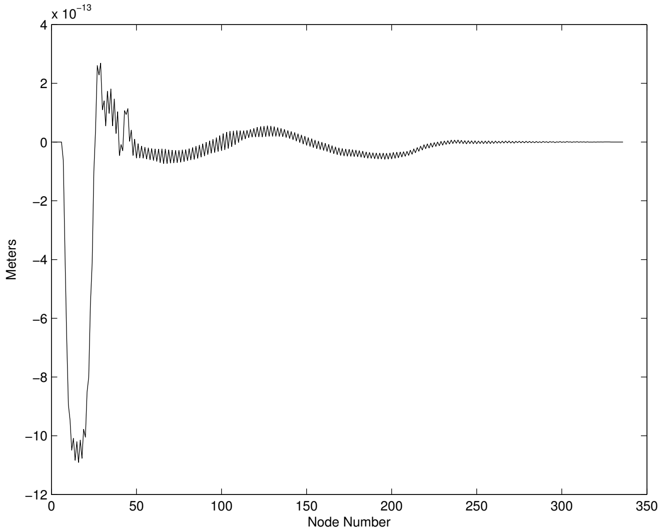

Figure 4.8

Distorsion of y values by transverse-twist coupling

4.2 Dispersion due to Material Stiffness

Material stiffness in beams causes dispersion [22]. The simulation has a feature to turn off stiffness so that we might compare the numerical dispersion with the material specific

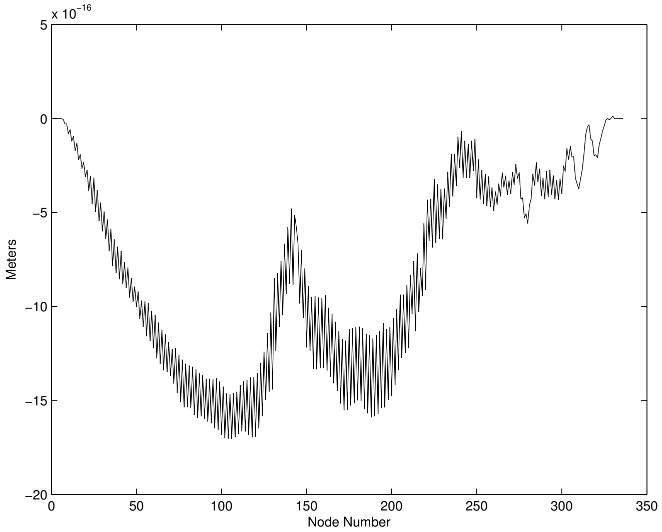

Figure 4.9

Distorsion of x values by transverse-twist coupling

dispersion. Figure 4.2 shows a pulse, traveling left to right, on a perfectly flexible beam. We see only a very small amount of dispersion as evidenced by the higher frequency ripples preceding the main pulse. Figure 4.11 shows the same pulse at the same time traveling on a stiff beam. Here we see that the numerical dispersion shown in Figure 4.2 is insignificant in comparison. This bodes well for the expectation that when material specific damping is included in the simulation that the numerical dissipation and dispersion will be orders of magnitude below the objective dissipation and dispersion.

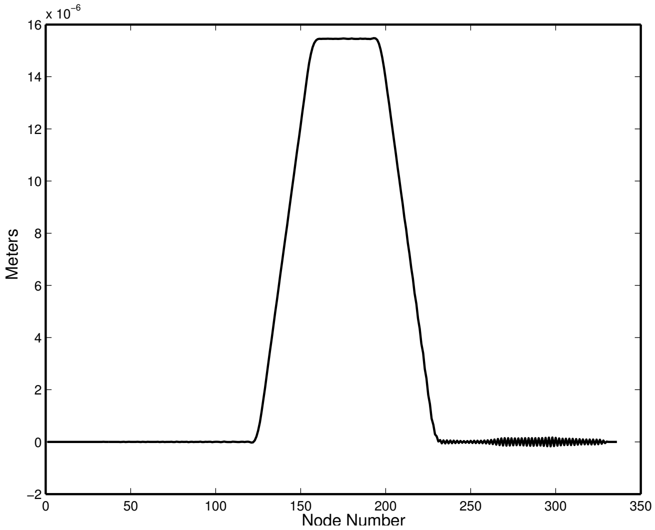

Figure 4.10

Dispersion due to numerical method

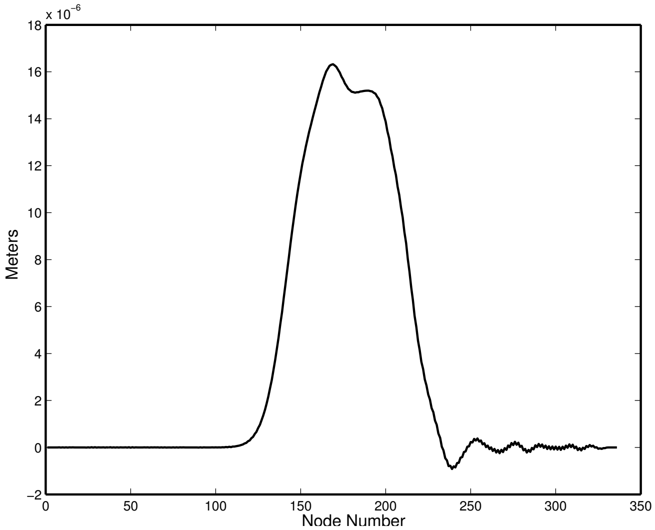

Figure 4.11

Dispersion due to material stiffness

CHAPTER 5

CONCLUSIONS AND FUTURE WORK

Capturing the astonishing behavior of a muscular hydrostat such as an octopus' arm requires the use of a complete 3D dynamic model. Furthermore, that complete 3D dynamic model must be solved. Therefore, to better develop robots which re-create these amazing abilities, this study presents the classical Cosserat rod coupled with a simple high-fidelity ($O(h^6)$) numerical solver which is suitable for parallelization or hardware implementation. Furthermore, the inherent numerical dissipation and dispersion are expected to be—a situation which cannot be tested without material specific damping—orders of magnitude below objective levels. No attempt, and thus no compromise, has been made towards real time applicability. The system is reasonably [1] conservative and reasonably stable and thus suitable as a test bed for future research.

Three specific limitations motivate future work:

1. Material specific damping,
2. Boundary condition solutions,
3. Fixed end free end scenarios.

Material specific damping is an absolute necessity for more robust stimulation, such as those involved with prey strike, as well as for any real world application. Boundary con-

---

[1] The system evidences a small numerical dissipation ($\Re(\xi) \approx 0.996$).

dition solutions are necessary for any scenario where both ends are not fixed or free as the present solution relies on a trick attained only with both ends treated identically and—to be of any practical use—the simulation must deal with tip loading (point forces) as well as the distributed loadings (body forces) such as gravity. Finally, the fixed end free end scenario is required to emulate the muscular hydrostats that have inspired this effort.

REFERENCES

[1] W. M. KIER and K. K. SMITH, "Tongues, tentacles and trunks: the biomechanics of movement in muscular-hydrostats," *Zoological Journal of the Linnean Society*, vol. 83, no. 4, pp. 307–324, 1985. [Online]. Available: http://dx.doi.org/10.1111/j.1096-3642.1985.tb01178.x

[2] R. J. Webster and B. A. Jones, "Design and kinematic modeling of constant curvature continuum robots: A review," *The International Journal of Robotics Research*, vol. 29, no. 13, pp. 1661–1683, 2010. [Online]. Available: http://ijr.sagepub.com/content/29/13/1661.abstract

[3] H. Kolsky, *Stress Waves in Solids*. New York: Dover Publication Inc., 2003.

[4] S. S. Antman, *Nonlinear problems of elasticity*, 3rd ed. New York: Springer Science+Business Media Inc., 2005.

[5] D. Trivedi, A. Lofti, and C. Rahn, "Geometrically exact models for soft robotic manipulators," *Robotics, IEEE Transactions on*, vol. 24, no. 4, 8 2008.

[6] H. Lang and M. Arnold, "Numerical aspects in the dynamic simulation of geometrically exact rods," Fraunhofer-Institut, Tech. Rep., June 2009.

[7] J. Spillman and M. Teschner, "Corde: Cosserat rod elements for the dynamic simulation of one-dimensional elastic objects," J. P. D. Metaxas, Ed. Eurographics/ACM SIGGRAPH Symposium on Computer Animation, 2007.

[8] H. Lang, J. Linn, and M. Arnold, "Multibody dynamics symulations of geometrically exact cosserat rods," K. A. J. Fraczek and M. Wojtyna, Eds. Warsaw, Poland: Multibody Dynamics 2009, ECCOMAS Thematic Conference, 6 2009.

[9] M. B. Rubin, "Numerical solution procedures for nonlinear elastic curved rods using the theory of a cosserat point," *Mathematics and Mechanics of Solids*, vol. 10, no. 1, pp. 89–126, 2005. [Online]. Available: http://mms.sagepub.com/content/10/1/89.abstract

[10] D. Rucker and R. Webster III, "Statics and dynamics of continuum robots with general tendon routing and external loading." Zurich, Switzerland: International Symposium on Experimental Robotics, 9 2010.

[11] B. Jones, R. Gray, and K. Turlapati, "Three dimensional statics for continuum robotics," in *Intelligent Robots and Systems, 2009. IROS 2009. IEEE/RSJ International Conference on*, 11 2009, pp. 2659 –2664.

[12] R. J. LeVeque, *Numerical methods for conservation laws*. Bassel Switzerland: Berhäuser Verlag, 2002.

[13] G. S. Chirikjian, "Hyper-redundant manipulator dynamics: A continuum approximation," *Advanced Robotics*, vol. 9, no. 3, pp. 217–243, 1995.

[14] I. A. Gravagne, C. D. Rahn, and I. D. Walker, "Large deflection dynamics and control for planar continuum robots," *IEEE/ASME Transactions on Mechanatronics*, vol. 8, no. 2, 6 2003.

[15] E. Tatlicioglu, I. Walker, and D. Dawson, "New dynamic models for planar extensible continuum robot manipulators," in *Intelligent Robots and Systems, 2007. IROS 2007. IEEE/RSJ International Conference on*, 11 2007, pp. 1485 –1490.

[16] M. Bergou, M. Wardetzky, S. Robinson, B. Audoly, and E. Grinspun, "Discrete elastic rods," in *ACM SIGGRAPH ASIA 2008 courses*, ser. SIGGRAPH Asia '08. New York, NY, USA: ACM, 2008, pp. 14:1–14:12. [Online]. Available: http://doi.acm.org/10.1145/1508044.1508058

[17] W. F. Ames, *Numerical methods for partial differential equations*. San Diego, California: Academia Press, 1992.

[18] K. F. Graff, *Wave motion in elastic solids*. New York: Dover Publications Inc., 1975.

[19] C. Zener, *Elasticity and Anelasticity of Metals*. Chicago: Chicago Press, 1948.

[20] E. Kreyszig, *Differential geometry*. New York: Dover Publication Inc., 1991.

[21] Daddario.com, "Violin tension chart," in *URL http://www.jdaddario.com/resources/JDCBOW/BOPK_Tension_Charts_Violin.pdf*.

[22] P. M. Morse and K. U. Ingard, *Theoretical Acustics*. Princeton New Jersey: Princeton University Press, 1968.